15A.6 Validation of NEXRAD Radar Differential Reflectivity in Snowstorms with Airborne Microphysical Measurements: Evidence for Hexagonal Flat Plate Crystals*

Earle Williams†, David Smalley, Michael Donovan, Robert Hallowell
Kenta Hood, Betty Bennett and Elaine Victoria
MIT Lincoln Laboratory

Mengistu Wolde, Matthew Bastian
Canadian National Research Council

Alexei Korolev
Environment Canada

Raquel Evaristo
Valparaiso University

1. INTRODUCTION

This study is concerned with the use of cloud microphysical aircraft measurements (the Convair 580) to verify the origin of differential reflectivity (ZDR) measured with a ground-based radar (the WSR-88D KBUF radar in Buffalo, New York). The underlying goal is to make use of the radar measurements to infer the presence or absence of supercooled water, which may pose an icing hazard to aircraft. The context of these measurements is the investment by the Federal Aviation Administration in the use of NEXRAD polarimetric radar and is addressed in the companion paper by Smalley *et al*. (2013, this Conference). The highlight of the measurements on February 28, 2013 was the finding of sustained populations of hexagonal flat plate crystals over a large area northwest of the KBUF radar, in conditions of dilute and intermittent supercooled water concentration. Some background discussion is in order prior to the discussion of the aircraft/radar observations that form the main body of this study. The anisotropy of hydrometeors, the role of humidity and temperature in crystal shape, and the common presence of hexagonal flat plate crystals in the laboratory cold box experiment are all discussed in turn.

1.1 Anisotropy of Hydrometeors

The hexagonal flat plate (HFP) crystal is particularly important to polarimetric radar work because it is the most anisotropic target among all common hydrometeors, solid and liquid. Theoretical studies (Hogan *et al*., 2002) have shown that hexagonal plates oriented horizontally in the gravity field can exhibit differential reflectivity as large as +9 dB. In contrast, the largest ZDR values expected for dendritic and needle-shaped crystals are +5 and +4 dB, respectively. Aircraft-based polarimetric studies with in situ verification of hydrometeor shapes have shown HFP crystals with ZDR values up to +7 dB (Wolde and Vali, 2001). In contrast, oblate raindrops of 5 mm size

---

† Corresponding Author: Earle Williams, MIT Lincoln Laboratory, 244 Wood Street, Lexington, MA 02420
e-mail: ***earlew@ll.mit.edu***

*This work was sponsored by the Federal Aviation Administration (FAA) under Air Force Contract FA8721-05-C-0002. Opinions, interpretations, conclusions, and recommendations are those of the author and are not necessarily endorsed by the United States Government.

(amongst the largest measured at the ground) show ZDR values of 4 dB (Teschl *et al*., 2008). Dendritic crystals growing at water-saturation can have aspect ratios as large as HFP crystals, but their maximum differential reflectivities are diminished because their 'porosity' is greater than zero (Vivekanandan *et al*., 1994).

Based on the foregoing considerations, HFP crystals are candidate radar targets whenever the ZDR values are in excess of +5 dB. This threshold is exceeded in the observations soon to be described.

1.2 Influence of Humidity and Temperature on Crystal Shape

Rich empirical information on the relationship between ice crystal habit and thermodynamic variables is available from diffusion chamber studies in the laboratory (Hallett and Mason, 1958; Bailey and Hallett, 2009). In this apparatus, both the temperature and the supersaturation can be precisely controlled. Figure 1 shows results on crystal shape versus temperature and humidity. Most cloud physics textbooks (e.g., Byers, 1965) maintain that temperature is the more important control variable on crystal shape, but a closer examination of Figure 1 in the range of relevance to winter storms (0 to -25 ^{o}C) shows otherwise. A distinct change in crystal form occurs at the water-saturation boundary for nearly all temperatures. At water sub-saturation, the growth is primarily two-dimensional, with HFPs dominant. At water supersaturation, the growth takes on a strongly one-dimensional character, with needles and dendrites prevalent, along with sector plates with more isolated sectors. While most published crystal diagrams (and especially the simplified versions of the same) show HFPs at water subsaturated conditions, the more detailed documentation in Figure 1 shows one HFP above the red water saturation boundary near -10 ^{o}C. This evidence will factor strongly in the interpretation of the aircraft observations of HFPs and supercooled water in Section 2.

1.3 Hexagonal Flat Plate Crystals in the Cold Box

The cloud seeding demonstration in a laboratory cold box, pioneered by V. Schaefer (Schaefer and Day, 1981) also has much relevance to this study. As Dr. Vincent Schaefer showed in a snowmaking demonstration in 1947 https://www.youtube.com/watch?v=2D5s2FlA_5k, and as shown in the experiments of Foster and Hallett (2008), HFP crystals are the predominant particle within the cold box. The unnaturally large ice crystal concentrations in seeded conditions, and the absence of a sustained lifting process in the cold box, together guarantee that the supercooled water concentrations are dilute or absent there. Such conditions appear to duplicate the natural conditions in which HFPs have been found in the aircraft observations reported in Section 2.

2. WINTER STORM AIRCRAFT OBSERVATIONS

2.1 Aircraft Platform

The in situ observations in this study were provided by the Convair 580 research aircraft operated by the National Research Council (NRC) of Canada. This two-engine aircraft has been designed for icing missions and is equipped with a full suite of cloud microphysical measurements, including supercooled water, hydrometeor phase, size and shape, plus the standard thermodynamic measurements. The supercooled water concentrations were measured independently with a King hot-wire sensor and with a Nevzorov probe. Complementary to these microphysical observations are an X-band and a W-band radar that operate continuously during the flight, with beams pointing upward, downward and perpendicular to the aircraft flight track.

2.2 Convair Flight on February 28, 2013

This flight was the third and final one in a sequence aimed at in situ icing verification in the vicinity of the NEXRAD KBUF radar in Buffalo, New York for comparison to the NEXRAD hydrometeor classifier. As noted in Smalley *et al*. (2013), many of the communication snags had been worked out in the previous two flights and this provided for nearly continuous 'chat' communication among Lincoln Laboratory personnel and the aircraft crew, as well as for the transfer of live radar images from the KBUF radar to the aircraft to aid in the decision making for flight tracks. This flight departed NRC in Ottawa at local noontime (1700 UTC) on a heading for Buffalo. The entire flight track is shown in Smalley *et al*. (2013, Figures 8 and 13). That portion of the flight track relevant to the surface radar comparisons discussed here is shown in Figure 2.

The Lincoln Laboratory team, with information on the aircraft location superimposed on KBUF radar imagery, identified an area of large positive differential reflectivity on the back edge of a precipitation region in the northwestern quadrant of the KBUF radar PPI (plan position indicator) display. The real time hydrometeor classification algorithm (HCA) was classifying this region as UK (Unknown). As the aircraft approached this region from the northeast, the optical glory phenomenon was observed repeatedly from the aircraft, supportive of the existence of liquid water in the cloud below.

Figure 2 shows the trajectory of the Convair in plan view, in the vicinity of the KBUF radar in Buffalo, over the two hour period (1757-1957 UTC). This trajectory shows the arrival from the NRC home base in Ottawa, Canada to the northeast, a series of NE/SW flight tracks back and forth through the region of large positive ZDR on the back side of the storm to the NW of the radar site, followed by an excursion to the east and southeast of the radar site to explore a region of stronger reflectivity (Z) closer to the leading edge of the system that continued its eastward migration throughout the flight. Also shown in Figure 2 are the trajectory sub-segments selected for expanded view in four-panel format (KBUF Z, KBUF ZDR, Convair LWC/T (liquid water content/temperature), and Convair particle shapes) in Figures 4 to 12.

The altitude of the aircraft was varying continuously during the trajectory shown in Figure 2, in an up-and-down ‘porpoising’ maneuver aimed at diagnosing vertical cloud structure, mainly between altitudes of 3500 ft/1.1 km (T = -6 ^{o}C) and 6100 ft/1.9 km (T = -11 ^{o}C) , and is depicted in Figure 3. This figure shows a time-height plot of the aircraft location (and with accompanying lat/long indexing), and includes information below the time axis on the dominant crystal shapes documented by the particle imaging probes during the flight, as well as the W-band reflectivity record in beams upward and downward from the aircraft location from the on-board radar. The W-band radar observations show reflectivity less than 5 dBZ from the crystal targets that likely dominate the radar return in the aircraft vicinity. More pronounced returns were encountered in both the aircraft W-band observations (Figure 3) and in the KBUF PPI scans later in the flight (1930-1940 UTC) when the stronger leading edge of the storm system was probed, and the aircraft ride was noticeably rougher. In the preceding period of porpoising in more quiescent conditions, the in situ temperatures of the lower and upper altitudes were -6 ^{o}C and -11 ^{o}C, and needle crystals predominated in the lower, warmer layer and hexagonal flat plate crystals predominated in the upper, colder layer. Measurements of supercooled water content show sustained levels in excess of 0.1 g/m^3 in the lower layer with needles and a generally smaller and more intermittent level in the upper layer with the hexagonal plate crystals. As shown in Figure 3, this pattern of alternating needles and plates was repeated four times, with needles evident in the lowest points of the trajectory and hexagonal plates evident in the upper layer over a horizontal distance of several tens of kilometers in Figure 2. This pattern is evidence for lateral homogeneity of the respective ice crystal populations over a large area of the storm.

A more detailed discussion of the subsegments of the flight trajectory identified in Figure 2, and detailed in the four-panel plots of Figures 4 to 12, is now appropriate. The time intervals for these subsegments vary from two to ten minutes, or in aircraft distance, 12 km to 60 km (at a nominal ground speed of 100 m/s). Each subsegment is documented in a four-panel plot with a radar reflectivity PPI in upper left, PPI of differential reflectivity in upper right, temperature and cloud water content time series in lower left, and a collection of particle imager results in lower right. In general, the selected subsegment of the flight trajectory is within +/- 0.5 degree of radar elevation angle of the selected PPI scans on which the flight track segments are superimposed.

As shown in the time-height plot in Figure 3, the Convair is descending from its ferrying altitude of ~5 km from 1735 to 1750 UTC. An initial sighting of the glory from the aircraft was noted at 1737 UTC and this phenomenon persisted throughout the descent in clear air and into the diffuse upper cloud. Ground observers following the aircraft location on the KBUF radar display anticipated entry into a region of high ZDR and on the right side of the aircraft, entirely consistent with the flight track in Figure 4 for the period 1759 to 1805 UTC which shows aircraft entry into the detectable reflectivity region on a SW heading. The real-time Hydrometeor Classification Algorithm (HCA) for this region assigned an 'Unknown' category over a large and contiguous region largely overlapping with the area of elevated differential reflectivity. (HCA will default to 'Unknown' when there are usable returns but no one classification category exceeds minimum interest.) Reflectivity values are weak and range from -18 to 0 dBZ and ZDR values vary from +1 to +7 dB. The in situ temperature is -10 ^{o}C at the observed time of the particle images and the liquid water content is small (<0.05 g/m^{3}) and intermittent. The observed crystals in the data from the 2DC probe are predominantly hexagonal plates. The angularity of the hexagonal shapes is often eroded in the imagery, suggesting some riming of the plates.

A few minutes later, in the time interval 1806 to 1809 UTC, the plane has progressed further southwest along the inside of the back edge of the precipitation system, but more in the gradient region of ZDR where values are 0 to +5 dB. The subsegment of the trajectory is documented in Figure 5. The reflectivity remains weak in the range of -12 to -3 dBZ. The HCA (not shown in Figure 5) classification is 'Unknown'. Supercooled water is small and intermittent. The in situ temperature is -8 ^{o}C. Crystals continue to be predominantly hexagonal flat plates.

By 1826 UTC, the plane is near the southwestern limit of its trajectory and reverses its direction to return to the radar features of interest now accessible via internet by the plane's pilot and co-pilot. This subsegment from 1826 to 1830 UTC is shown in Figure 6. This period represents the largest ZDR region intersected by the aircraft during the flight. Values in the white region (+5 to +8 dB) are evident here, where the Z values are weak (-15 to -7 dBZ). Hexagonal flat plate crystals remain the dominant hydrometeor in the 2DC display, at a temperature near -9 ^{o}C. The HCA classification is again 'Unknown'. The aircraft is descending at this time (and hence the temperature is increasing) in its porpoising maneuver and by 1832 UTC again attains minimum altitude. Figure 7 documents the time period 1832-1834 UTC when the aircraft is for a second time immersed in a predominance of needle-shaped crystals, with an in situ temperature of -4.5 ^{o}C. The reflectivity in this region is somewhat larger, in the range of -10 to 3 dBZ and the ZDR values in the range of -3 to +2 dB are significantly less than the values documented in regions populated with hexagonal flat plates. The HCA shows a mix of 'Unknown' and 'Dry snow', both inconsistent with the clearly defined documentation in the in situ observations. The liquid water content is sustained over time in this region and is larger than what is generally observed in the upper level with the plates, reaching maximum values of 0.3 g/m^{3}.

The period of glory observation from the aircraft looking down on the cloud was sustained (with a few breaks) for the period 1735-1803 UTC (also shown in Figure 3). The dominant origin for this glory is most likely the richer supercooled layer co-located with the needle crystals at a temperature near -6 ^{o}C and height of about 1 km.

The aircraft is headed northeast again for the interval 1835 to 1839 UTC, and this subsegment is documented in Figure 8. According to Figure 3, the aircraft again attains maximum altitude (1.9 km) and minimum temperature (-10 ^{o}C) in this time interval, at about 1837 UTC. The location is again on the forward edge of the anomalous positive ZDR region, in a background of light reflectivity in the range of -15 to +7 dBZ and with ZDR values in the 0 to +6 dB range. The HCA (not shown) again indicates a broad region of 'Unknown'. The liquid water content is small (mean 0.07 g/m^3) and intermittent, and the dominant crystals are again hexagonal plates.

During the time interval 1843 to 1850 UTC, the Convair attains a northern maximum (at 1846 UTC) and then reverses direction. While making this left hand turn, the plane is located in another maximum of differential reflectivity, with red values in Figure 9 (upper right) reaching +8 dB. The temperature is -11 ^{o}C and the supercooled water concentration is intermittent, sometimes completely absent but also attaining a maximum value of 0.16 g/m^3, and once again hexagonal plates completely dominate the hydrometeor populations. The HCA categorization is 'Unknown'. At the northern edge of the radar reflective region, the return at the aircraft location is in the range -19 to -6 dBZ. In moving south and descending again to a minimum altitude at 1855 UTC (Figure 3), the consistent layer of needles is found again, over the time interval 1852-1854 UTC documented in the four-panel plot of Figure 10. The HCA categorization (not shown) is a mixture of 'Unknown', 'Dry Snow', and 'Ice Crystals'. The supercooled water concentration is again larger (0.2-0.3 g/m^3) and more persistent in the presence of needles than in the presence of hexagonal plates. Consistent with earlier comparisons, the differential reflectivity of the needles lies in the range of +0 to +4 dB, consistently less than that for the hexagonal plates. The background reflectivity lies in the range of -5 to +16 dBZ.

At the urging of both the ground observers and based on information that stronger radar returns also with anomalous differential radar reflectivity lay to the southeast of the aircraft location, the aircraft then headed due east at 1916 UTC to a location southeast of the KBUF radar location, as shown in Figure 2. Then during the interval 1927 to 1930 UTC, a region with predominance of dendritic shapes and crystal aggregates was probed, with documentation in four-panel Figure 11. The reflectivity along this subsegment is larger (-2 to 10 dBZ) than most previously discussed segments. (This is also shown by the on-board X-band radar evidence in Figure 3.) The differential reflectivity in this interval, dominated by dendritic crystals, lies in the range of +2 to +7 dB, larger than values for needles but smaller than values documented earlier with the hexagonal plates. The HCA classification is again 'Unknown'. Similar ZDR values with dendritic crystals were documented in another storm described by Williams *et al*. (2013). The in situ temperature at the time of the particle observations is -12 ^{o}C and the supercooled water concentration is highly variable but attains a maximum value of ~0.4 g/m^3, close to the maximum value for the entire flight.

The final region probed (from 1949 to 1952 UTC) is also populated primarily by dendritic crystals and aggregated crystals, as shown in the four-panel documentation in Figure 12. The radar reflectivity here lies in the range 9 to 19 dBZ, and in comparison with the larger ZDR values associated with flat plate crystals, the values in this region are +1 to +5 dB. The HCA categorization is a mix of 'Dry snow' and 'Unknown', still flawed relative to the aircraft verification. The aircraft is ascending in this interval and so the temperature is declining, with a value of -9 ^{o}C at the time of the particle observations. The supercooled water concentration is again highly variable, with a maximum value of ~0.2 g/m^3.

3. DISCUSSION

The storm system of February 28, 2013 probed by aircraft northwest of the KBUF radar showed evidence for laterally extensive layers of weak radar reflectivity (generally < 0 dBZ) in which a single shape of ice crystal predominated, with needles dominant at an in situ temperature near -6 ^{o}C and hexagonal flat plate crystals near -11 ^{o}C. The latter crystals are often close to 1000 µm in diameter, with estimated fall speeds of only ~0.5 m/s, and so a time period of ~1 hour is needed for the plates to descend to the lower needle layer to mix things up. The more vigorous and strongly reflective (~20 dBZ) leading portion of the storm to the southeast of the radar showed a predominance of dendritic crystals in a slightly lower range of temperature (-9 to -12 °C).

The differential reflectivity measurements for the three crystal types are broadly consistent with theoretical calculations (e.g., Hogan *et al*., 2002) showing positive values of ZDR for all shapes, and largest magnitudes for plates, intermediate values for dendrites and least values for needles, as indicated in Table 1.

Table 1. Summary of observed crystal types, in situ measurements and radar comparisons

Crystal type	**Temperature range**	**Height range**	**Z range**	**ZDR range**	**LWC**
Needles	-4° to -6° C	0.8 to 1.3 km	-10 to 16 dBZ	+2 to +4 dB	0.1-0.3 g/m^3 (sustained)
Hexagonal plates	-10° to -11° C	1.3 to 2.0 km	-18 to +7 dBZ	+4 to +8 dB	<0.1 g/m^3 (intermittent)
Dendrites/ aggregates	-9° to -12° C	0.8 to 2.0 km	-2 to 19 dBZ	+2 to +7 dB	0 – 0.4 g/m^3 (intermittent)

The hexagonal flat plate radar targets can be classified in the Category B of our earlier study (Williams *et al*., 2011), in the sense that the differential reflectivity is large (+8 dB, at the limit of the NEXRAD recording range for ZDR) and the reflectivity quite small (<0 dBZ), and is consistently most pronounced near the edge of the detectable reflectivity. Radar returns of this sort are best observed using a NEXRAD ‘clear air’ scan strategy. This rather extreme polarimetric radar characterization may account for the categorization of ‘Unknown’ in the real-time HCA depiction for this storm. This Category B case is however characterized by the presence of supercooled water. Though the LWC is small (<0.1 g/m^3) and does not pose a grave icing hazard, it is still measureable by the aircraft. The intermittent nature of the supercooled water in all zones showing hexagonal flat plates may account for the straddling of HFPs on the water saturation boundary, according to the controlled measurements in laboratory diffusion chambers (Figure 1).

The three crystal types are found in temperature regions consistent with the expectations based on diffusion chamber measurements of Figure 1 (Bailey and Hallett, 2009). The needles are also found in sustained supercooled water, consistent with the expected water-saturation condition in the diffusion chamber. The finding of dendrites in the presence of supercooled water is also consistent with the diffusion chamber data.

The results of this analysis suggest an additional approach for NEXRAD dual-pol-based icing hazard detection that could be included in the NEXRAD Icing Hazard Levels product (Hallowell *et al*., 2013). Generally, light and intermittent icing conditions were found at altitudes above water saturated conditions where notably more LWC was present. The three-dimensional structure as such was associated with different crystal types and prevalence of riming. In turn, that was associated with different radar combinations of Z and ZDR especially. A technique to assess such structure over a range in altitude could be developed leading to expanded icing hazard identification, and remedying the persistent ‘Unknown’ HCA categorization problem. Further study is needed of the radar combinations to distinguish LWC (water-saturated conditions) from subsaturated regions.

4. CONCLUSIONS

The existence of large winter precipitation regions with predominantly single ice crystal type on February 28, 2013 provided an excellent opportunity to validate the ground-based polarimetric radar measurements with the aircraft observations. The largest sustained supercooled water concentrations were co-located with needles, with smaller, intermittent concentrations coinciding with hexagonal flat plates and dendritic crystals. The finding of extensive regions of hexagonal plate crystals is a rare occurrence for cloud physics aircraft measurements. In this case the aircraft was directed to this region on the basis of the telltale signature of large positive differential reflectivity in ground-based polarimetric radar observations. Both the quiescence and the isolation of the region of interest in the trailing portion of the storm may have been responsible for quasi-homogeneous conditions needed for initiation and growth of the hexagonal flat plate form.

5. ACKNOWLEDGEMENTS

We thank Steve Kim, Tom Webster, and Bill Bumgarner of the FAA NEXRAD Program Office for encouragement and support. We are also indebted to the pilot Paul Kissman and flight crew (Anthony Brown, Matthew Bastian, Gary Giles, Steve Ingram and Mohamed Wasey) of the NRC Convair 580 for several successful missions. Discussions on microphysical aspects with Andy Detwiler, John Hallett, Danny Rosenfeld, Steve Rutledge and Tsutomu Takahashi are much appreciated.

6. REFERENCES

Bailey, M.P. and J. Hallett, A comprehensive habit diagram for atmospheric ice crystals: Confirmation from the laboratory, AIRS II and other field studies, J. Atmos. Sci., 66, 2888-2899, 2009.

Byers, H.R., Elements of Cloud Physics, University of Chicago Press, 1965, 191 pp.

Foster, T.C. and J. Hallett, Enhanced alignment of plate ice crystals in a non-uniform electric field, Atmos. Res., 90, 41-53, 2008.

Hallett, J. and B.J. Mason, The influence of temperature and supersaturation on the habit of ice crystals grown from the vapor, Proc. Roy. Soc., A247, 440-453, 1958.

Hallowell, R. G., M. F. Donovan, D. J. Smalley, and B. J. Bennett, 2013: Icing Hazard Detection with NEXRAD IHL. *Proc. American Meteorological Society's 36th International Radar Conference, Breckenridge, CO.*

Hogan, R.J., P.R. Field, A.J. Illingworth, R.J. Cotton, and T.W. Choularton, Properties of embedded convection in warm-frontal mixed-phase cloud from aircraft and polarimetric radar data, Q.J.R.M.S., 128, 451-476, 2002.

Schaefer, V.J. and J.A. Day, A Field Guide to the Atmosphere, Houghton Mifflin Company, Boston, 1981, 359 pp.

Smalley, D.J., E.R. Williams, M.F. Donovan, R.G. Hallowell, K.T. Hood, B.J. Bennett, M. Wolde, M. Bastien, and A. Korolev, In situ icing verification, *Proc. American Meteorological Society's 36th International Radar Conference, Breckenridge, CO*.

Teschl, F., W.L. Randeu, M. Schönhuber, and R. Teschl, Simulation of polarimetric radar variables in rain at S-, C-, and X-band wavelengths, Adv. Geosci., 16, 27-32, 2008.

Vivekanandan, J., V.N. Bringi, M. Hagen and P. Meischner, Polarimetric radar studies of atmospheric ice particles, IEEE Transactions on Geoscience and Remote Sensing, 32, 1-9, 1994.

Williams, E.R., D.J. Smalley, M.F. Donovan, R.G. Hallowell, K.T. Hood, B.J. Bennett, R. Evaristo, A. Stepanek, T. Bals-Eisholz, J. Cobb and J.M. Ritzman, Dual polarization radar winter storm studies supporting development of NEXRAD-based aviation hazard products, Proc. American Meteorological Society's 35th International Radar Conference, Pittsburgh, PA., September, 2011.

Williams, E.R., D. J. Smalley, M.F. Donovan, R.G. Hallowell, K.T. Hood, B.J. Bennett, R. Evaristo, A. Stepanek, T. Bals-Elsholz, J. Cobb, J. Ritzman, A. Korolev, and M. Wolde, Measurements of differential reflectivity in snowstorms and warm season stratiform systems, JCAM (submitted, August, 2013).

Wolde, M., and G. Vali, Polarimetric signatures from ice crystals observed at 95 GHz in winter clouds, Part I: Dependence of crystal form, J. Atmos. Sci., 58, 828-841, 2001.

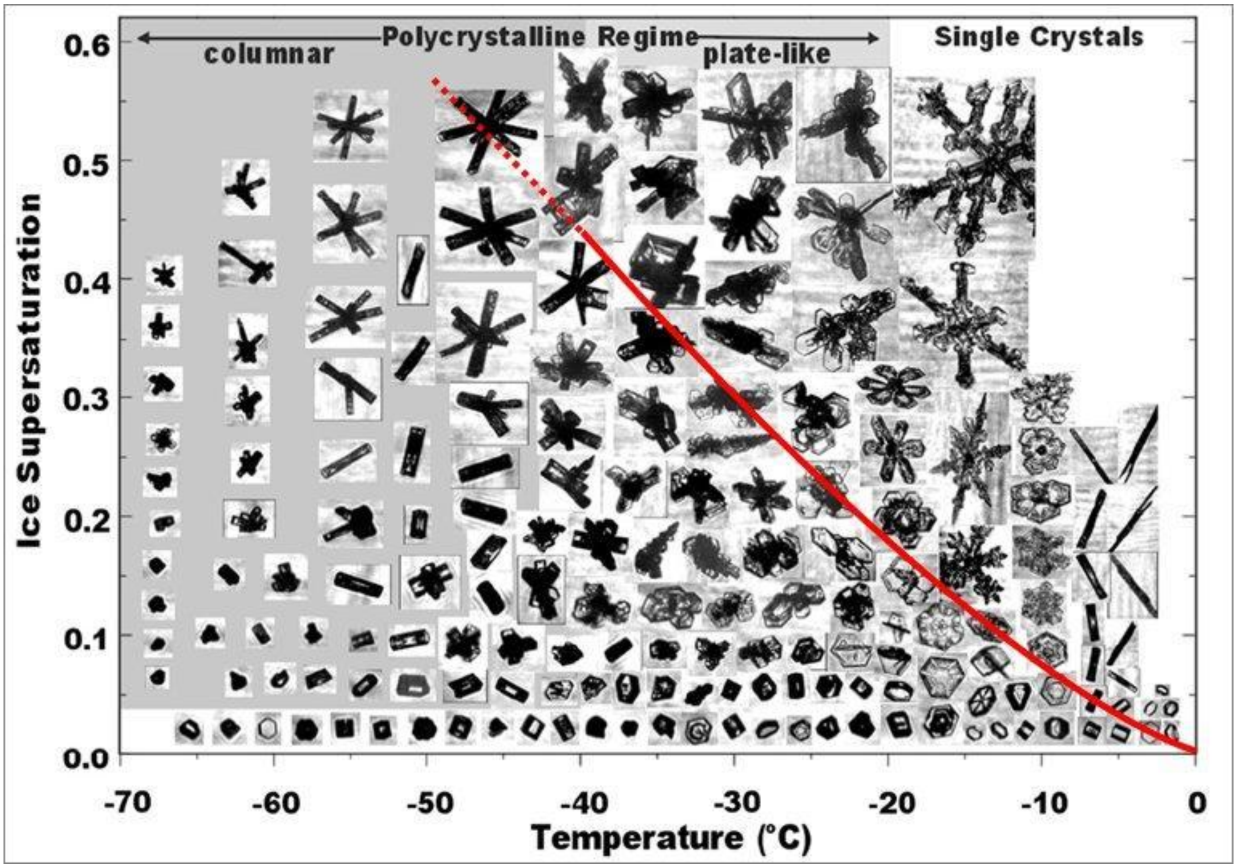

Figure 1. Illustration of the variability of ice crystal shapes documented in a laboratory diffusion chamber in which humidity and temperature are stringently controlled (from Bailey and Hallett, 2009). The water-saturation boundary is shown in red. One hexagonal flat plate crystal is evident near -10 ^{o}C and above the water-saturation boundary.

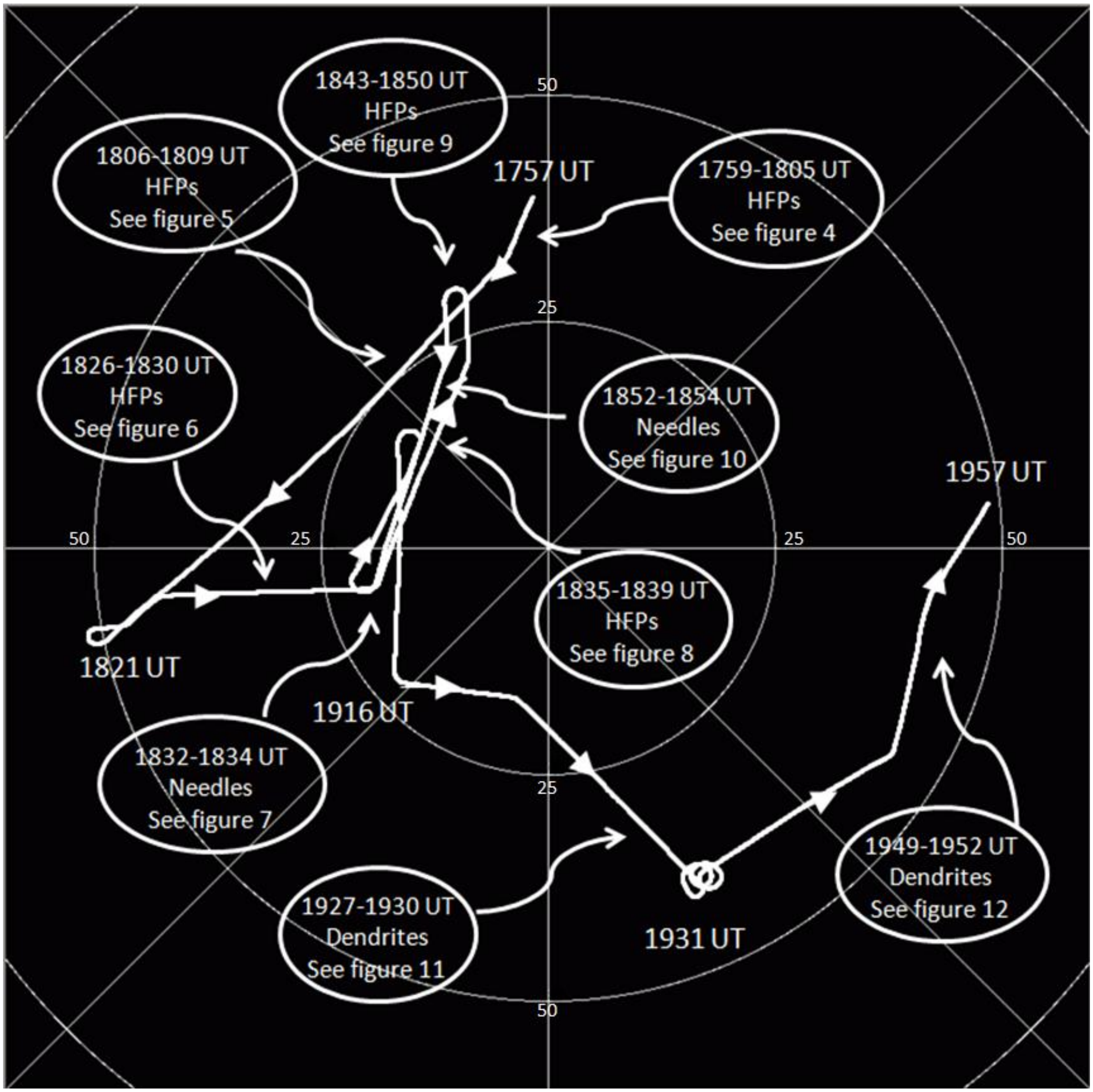

Figure 2. Plan view of the Convair 580 aircraft trajectory in the vicinity of the WSR-88D KBUF polarimetric S-band radar (in Buffalo, New York) on February 28, 2013 from 1757 to 1957 UTC. Radar range rings are shown at 25 and 50 nm. The time intervals of all the shorter subsegments of this trajectory that receive detailed documentation in Figures 4 to 12 are also marked. The crystal type for each subsegment is noted (HFPs are Hexagonal Flat Plates).

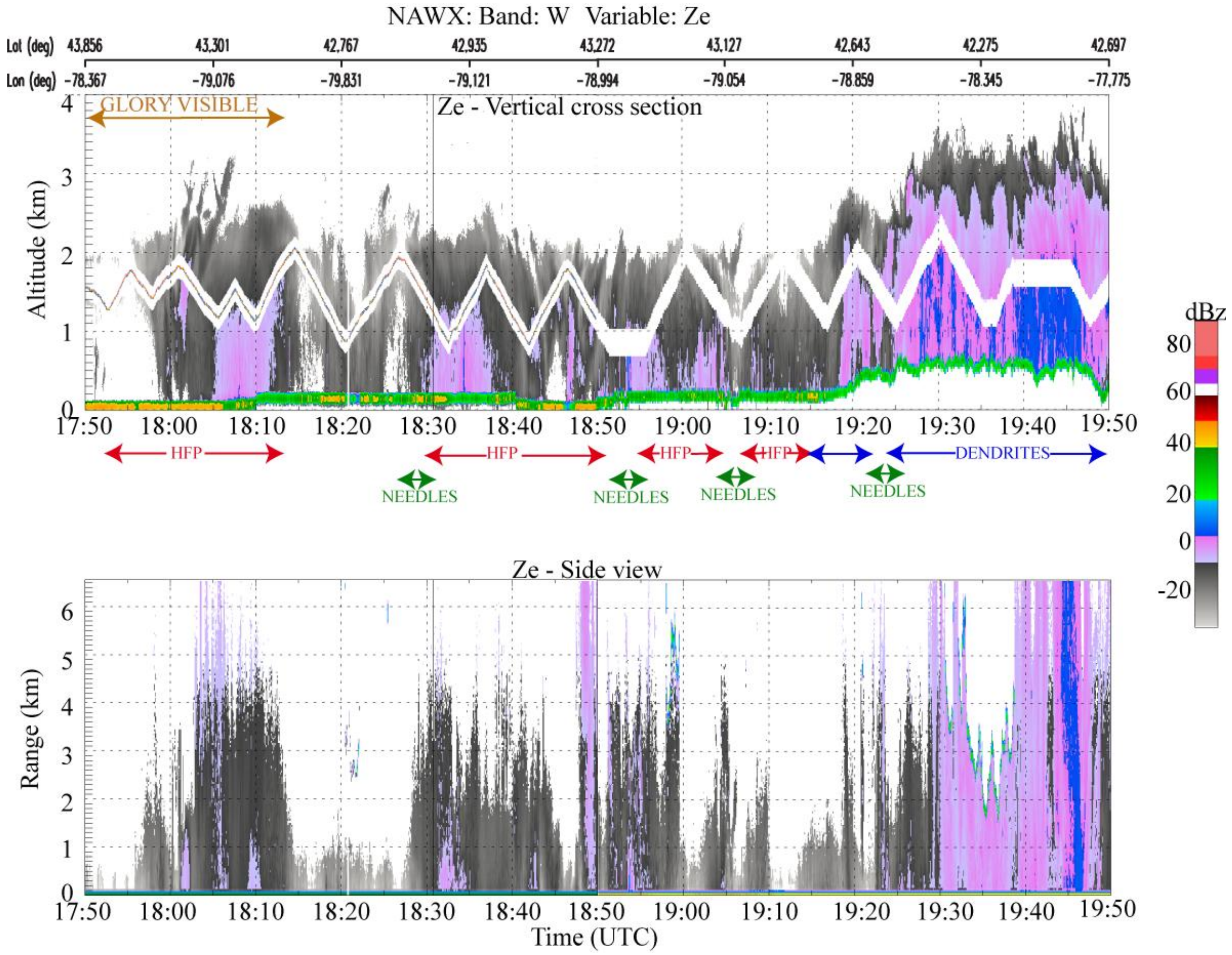

Figure 3. Time-height plot of the Convair flight shown in Figure 2, illustrating the alternation between maximum and minimum altitudes in a porpoising maneuver. The on-board W-band radar observations are also shown. The time periods of particular ice crystal predominance are shown. The period of glory observation from the aircraft (1735-1803 UTC) is also shown. HFP represents hexagonal flat plates.

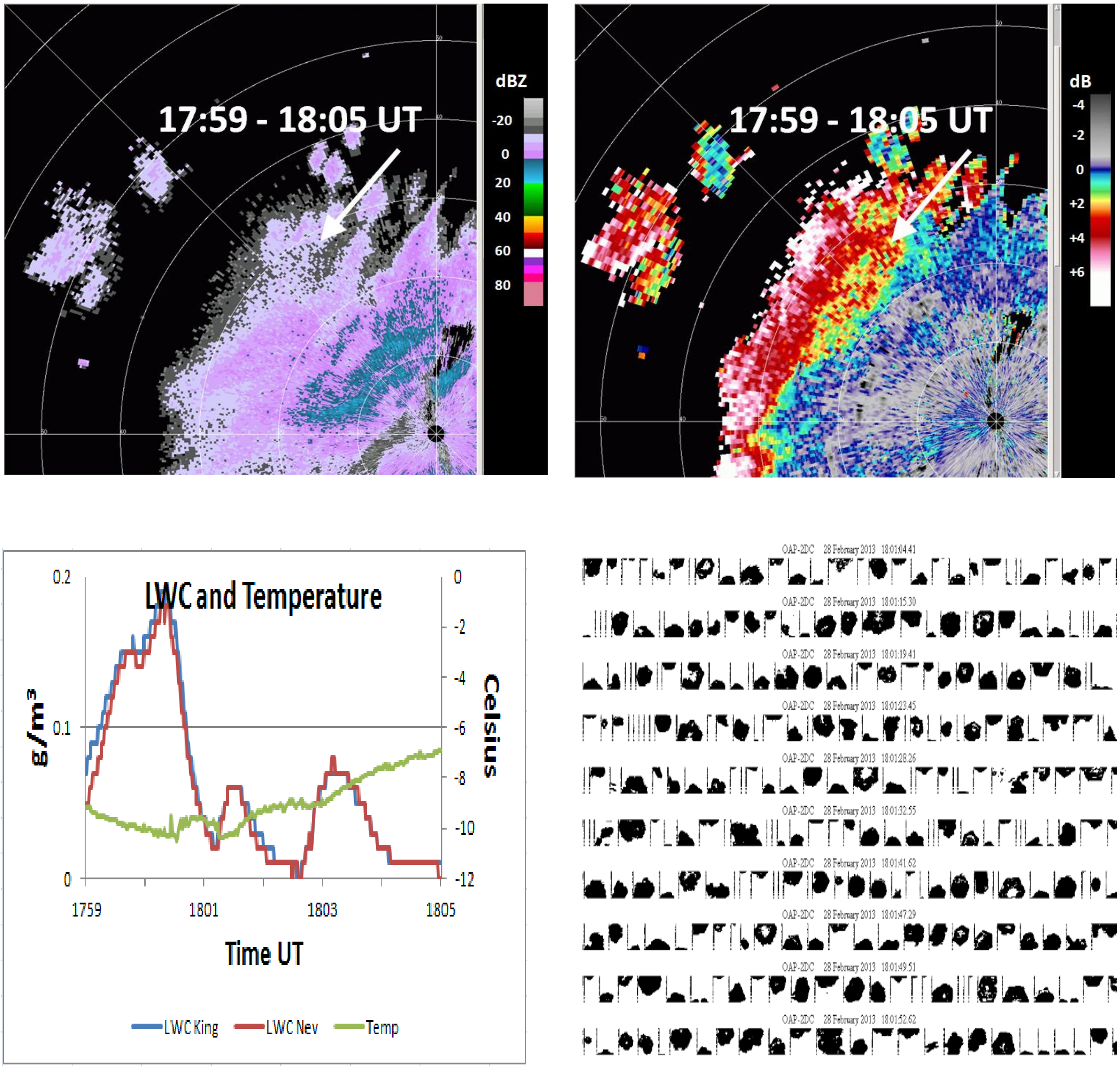

Figure 4. Four-panel plot documenting the Convair aircraft sample time interval 1759-1805 UTC, and including space-time-matched KBUF radar reflectivity Z(upper left), differential reflectivity ZDR (upper right), in situ liquid water content (g/m^3) and temperature (^{o}C) (lower left), and ice particle PMS 2DC imagery (lower right), with pixel resolution 25 µm and spacing between vertical lines 800 µm. Hexagonal flat plate crystals are the predominant hydrometeor type at this time, and the co-located ZDR values are +1 to +7 dB. Some riming of the hexagonal plates is evident. Z and ZDR panel for elevation angle 1.5^o with range ring labels in nautical miles.

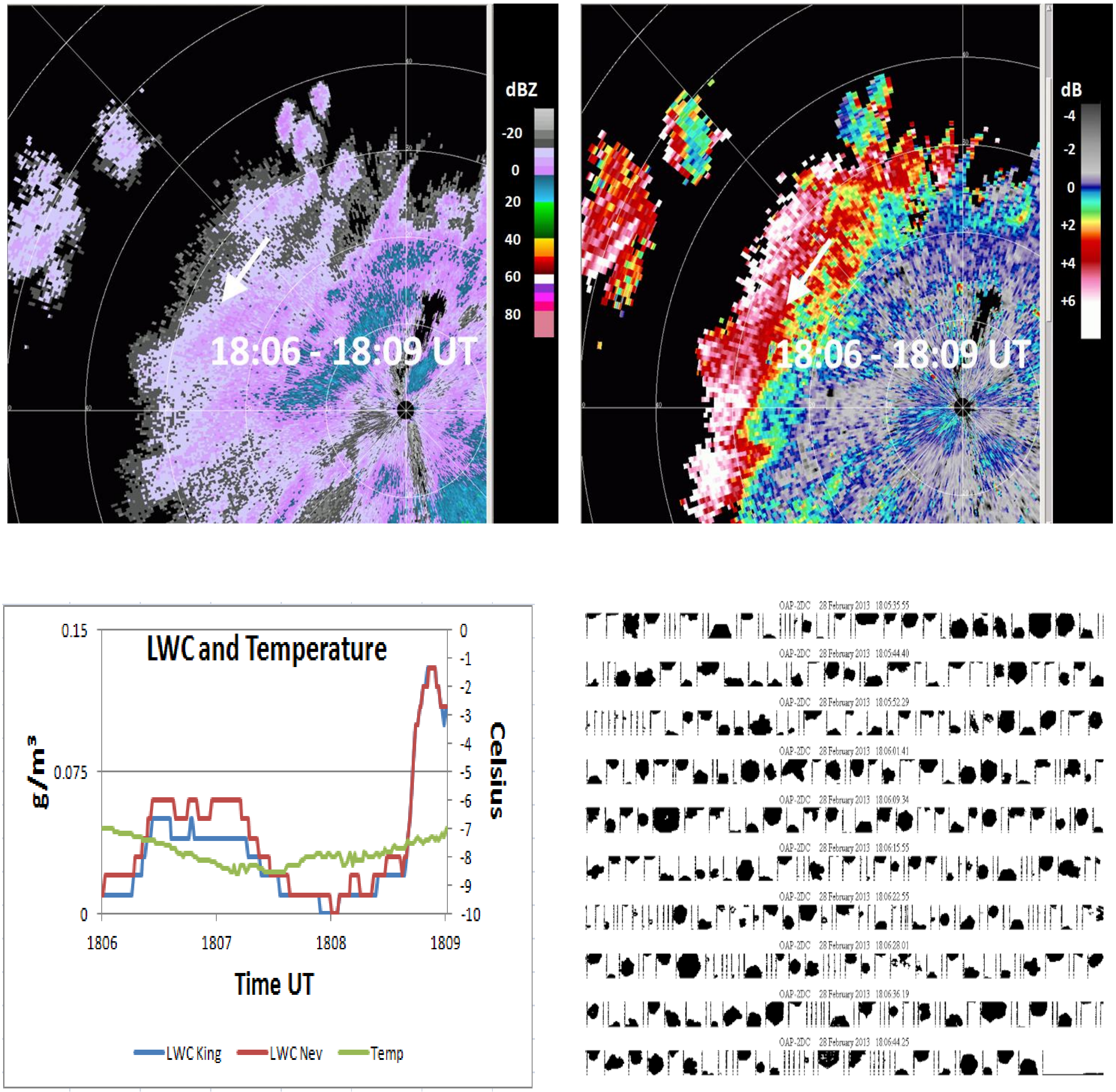

Figure 5. Four-panel plot documenting the Convair aircraft sample time interval 1806-1809 UTC, and including space-time-matched KBUF radar reflectivity Z (upper left), differential reflectivity ZDR (upper right), in situ liquid water content (g/m^3) and temperature (^{o}C) (lower left), and ice particle PMS 2DC imagery (lower right), with pixel resolution 25 µm and spacing between vertical lines 800 µm. Hexagonal flat plate crystals are the predominant hydrometeor type at this time, and the co-located ZDR values are 0 to +5 dB. The angular features of many hexagonal plates are well defined, but in some cases, riming is evident. Z and ZDR panel for elevation angle 1.5^o with range ring labels in nautical miles.

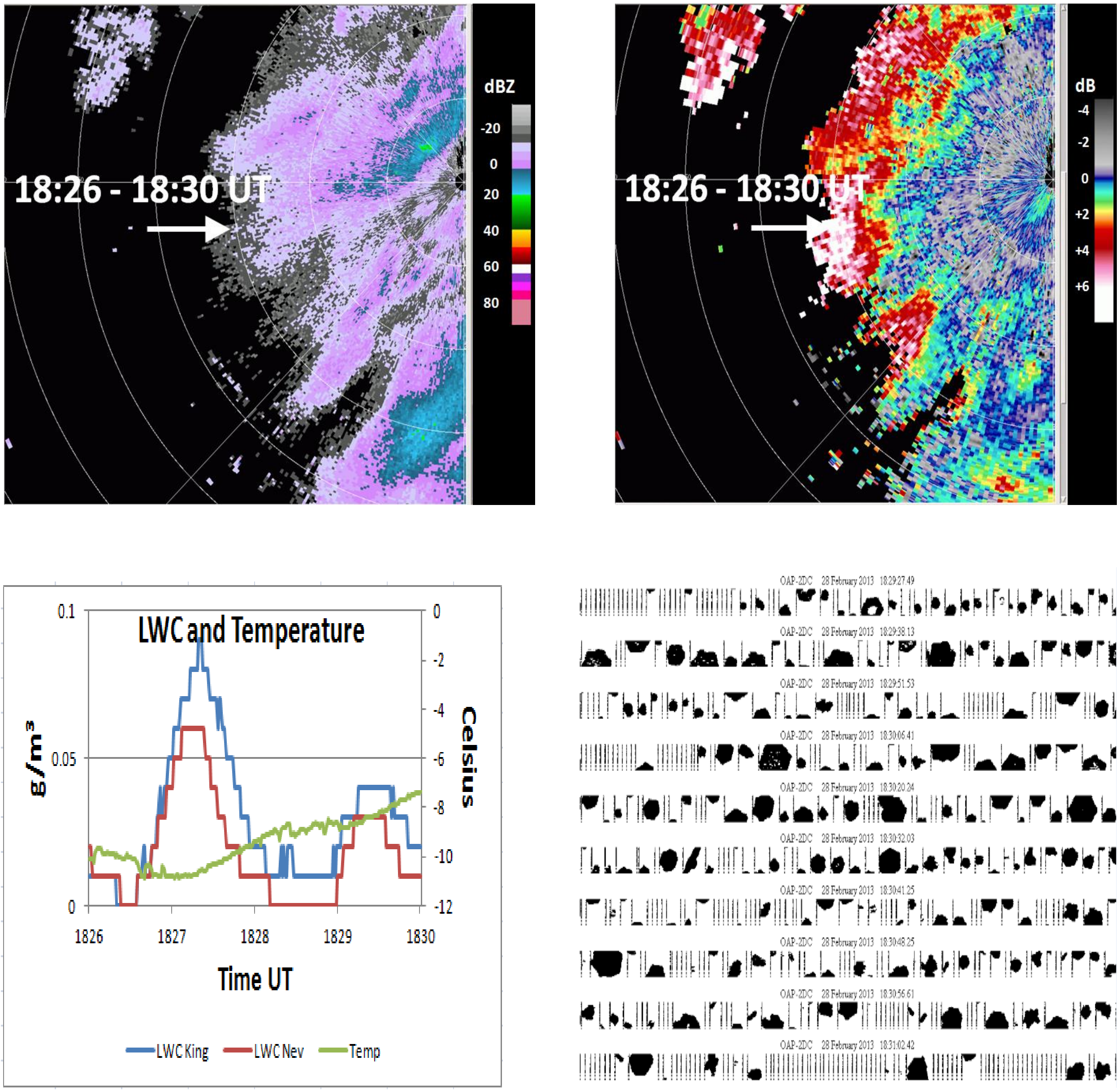

Figure 6. Four-panel plot documenting the Convair aircraft sample time interval 1826-1830 UTC, and including space-time-matched KBUF radar reflectivity Z (upper left), differential reflectivity ZDR (upper right), in situ liquid water content (g/m^3) and temperature (^{o}C) (lower left), and ice particle PMS 2DC imagery (lower right), with pixel resolution 25 µm and spacing between vertical lines 800 µm. Hexagonal flat plate crystals are the predominant hydrometeor type at this time, and the co-located ZDR values are +5 to +8 dB. Several of the largest hexagons are sharply defined, but rounded corners on others are indicative of riming. Z and ZDR panel for elevation angle 1.5^o with range ring labels in nautical miles.

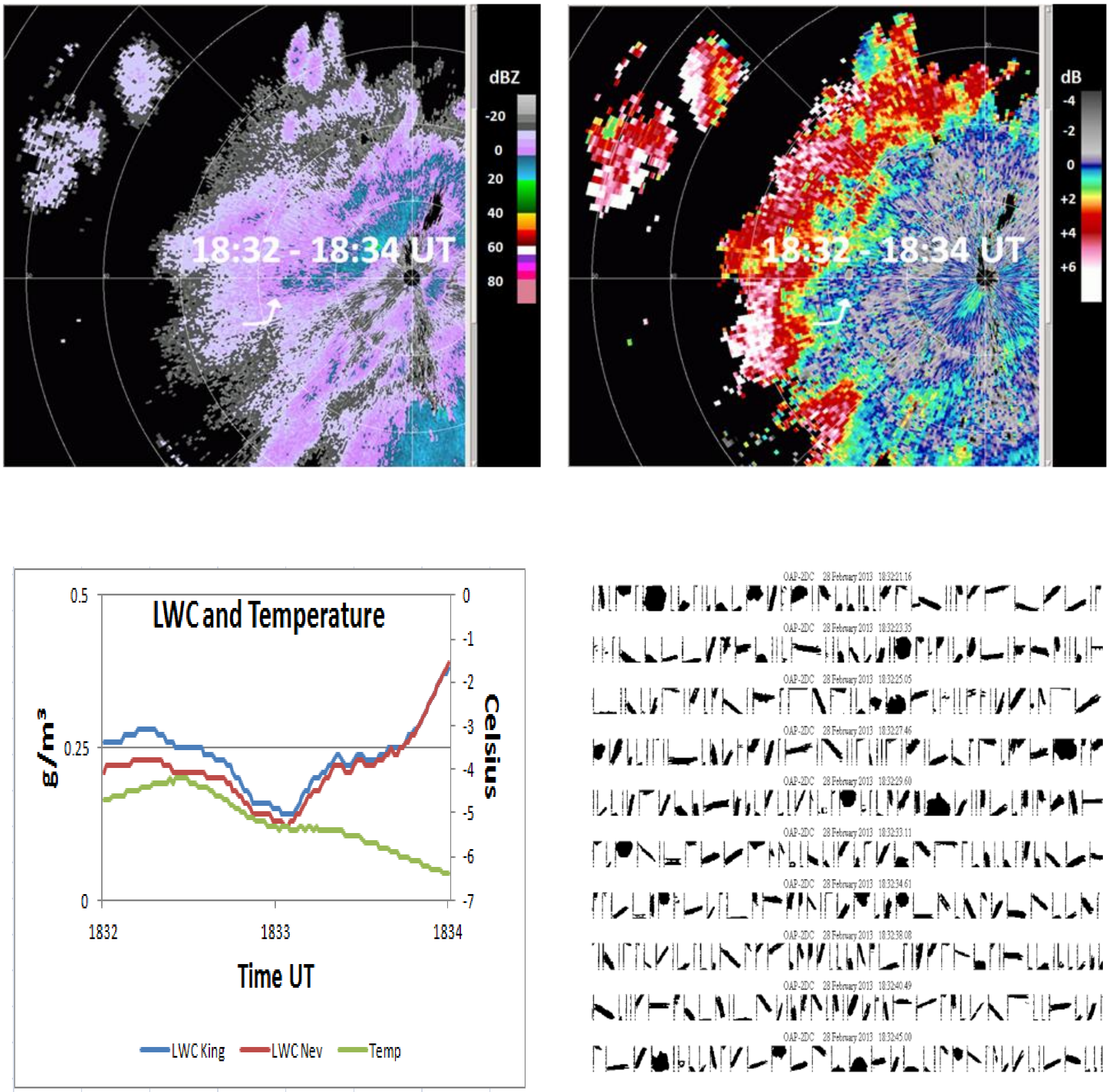

Figure 7. Four-panel plot documenting the Convair aircraft sample time interval 1832-1834 UTC, and including space-time-matched KBUF radar reflectivity Z (upper left), differential reflectivity ZDR (upper right), in situ liquid water content (g/m^3) and temperature (^{o}C) (lower left), and ice particle PMS 2DC imagery (lower right), with pixel resolution 25 µm and spacing between vertical lines 800 µm. Needles are the predominant hydrometeor type at this time, and the co-located ZDR values are -3 to +2 dB. The resolution of the particle imagery (25 µm per pixel) is insufficient to identify riming unambiguously, but riming is suspected. Z and ZDR panel for elevation angle 1.5^o with range ring labels in nautical miles.

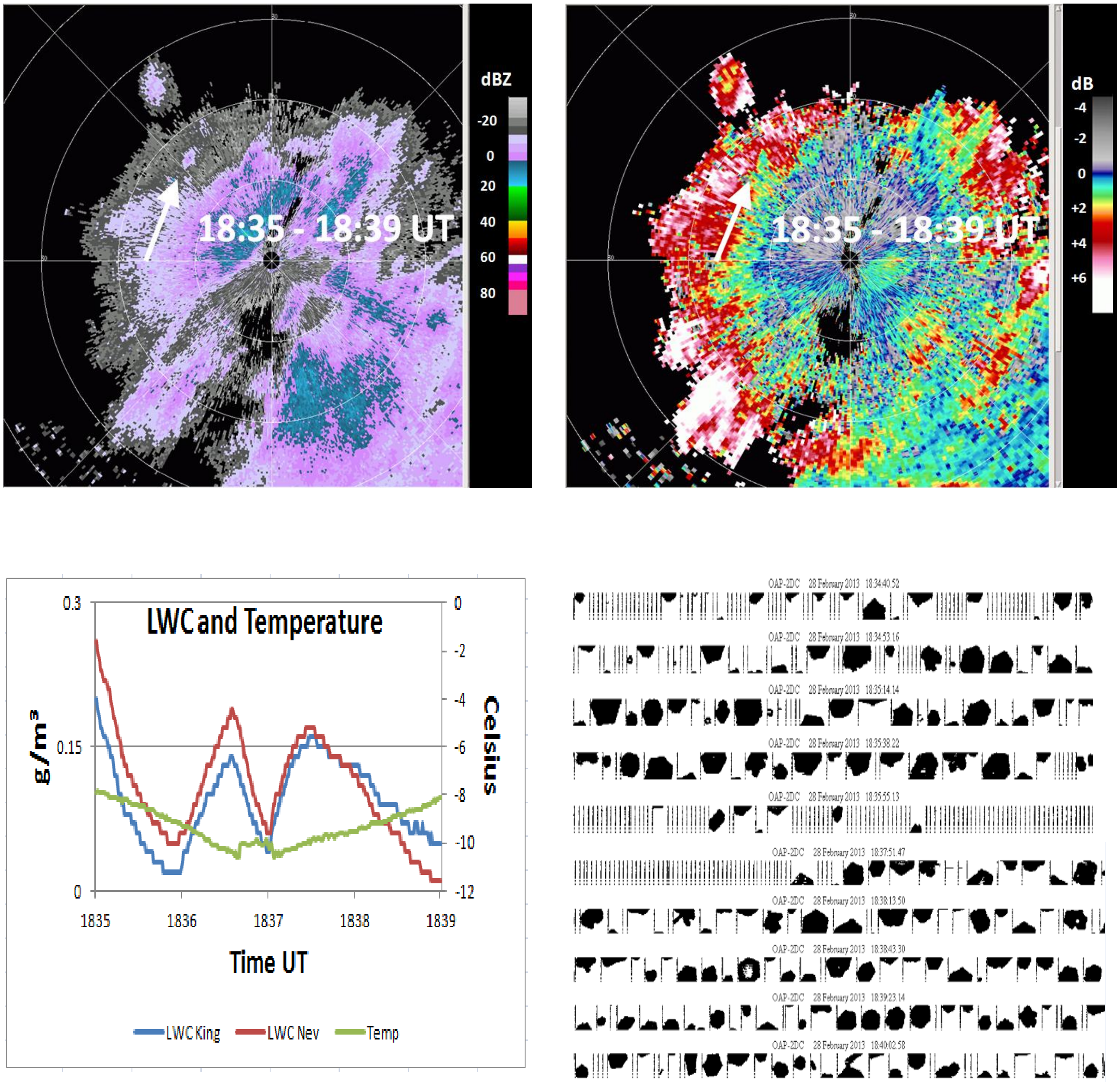

Figure 8. Four-panel plot documenting the Convair aircraft sample time interval 1835-1839 UTC, and including space-time-matched KBUF radar reflectivity Z (upper left), differential reflectivity ZDR (upper right), in situ liquid water content (g/m^3) and temperature (^{o}C) (lower left), and ice particle PMS 2DC imagery (lower right), with pixel resolution 25 µm and spacing between vertical lines 800 µm. Hexagonal flat plate crystals are the predominant hydrometeor type at this time, and the co-located ZDR values are 0 to +6 dB. Rounded corners on many of the hexagons suggest riming of these plates. Z and ZDR panel for elevation angle 2.5^o with range ring labels in nautical miles.

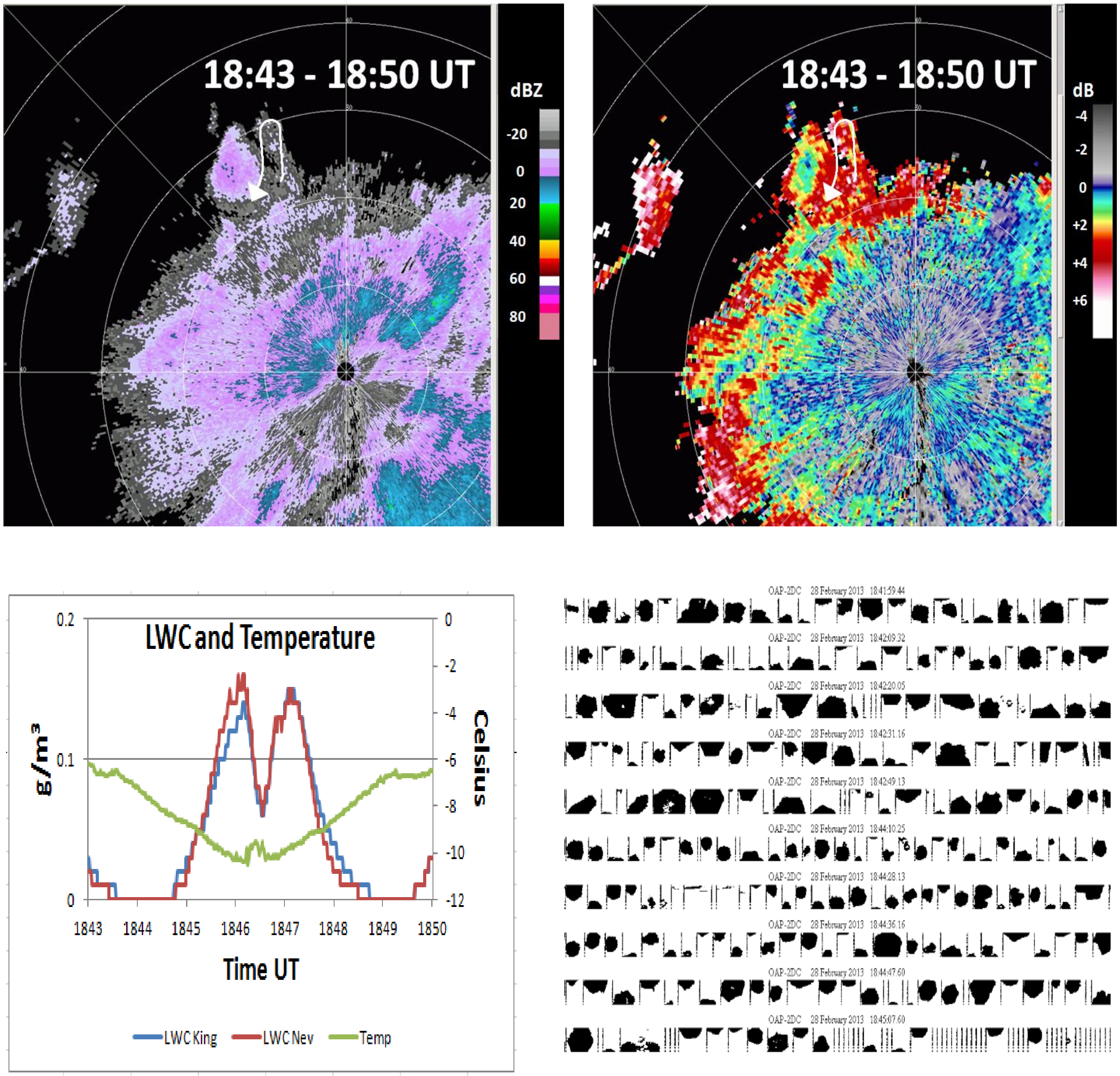

Figure 9. Four-panel plot documenting the Convair aircraft sample time interval 1843-1850 UTC, and including space-time-matched KBUF radar reflectivity Z (upper left), differential reflectivity ZDR (upper right), in situ liquid water content (g/m^3) and temperature (^{o}C) (lower left), and ice particle PMS 2DC imagery (lower right), with pixel resolution 25 µm and spacing between vertical lines 800 µm. Hexagonal flat plate crystals are the predominant hydrometeor type at this time, and the co-located ZDR values are as large as +8 dB. Many hexagons are well defined, but some have rough edges suggestive of riming. Z and ZDR panel for elevation angle 1.5^o with range ring labels in nautical miles.

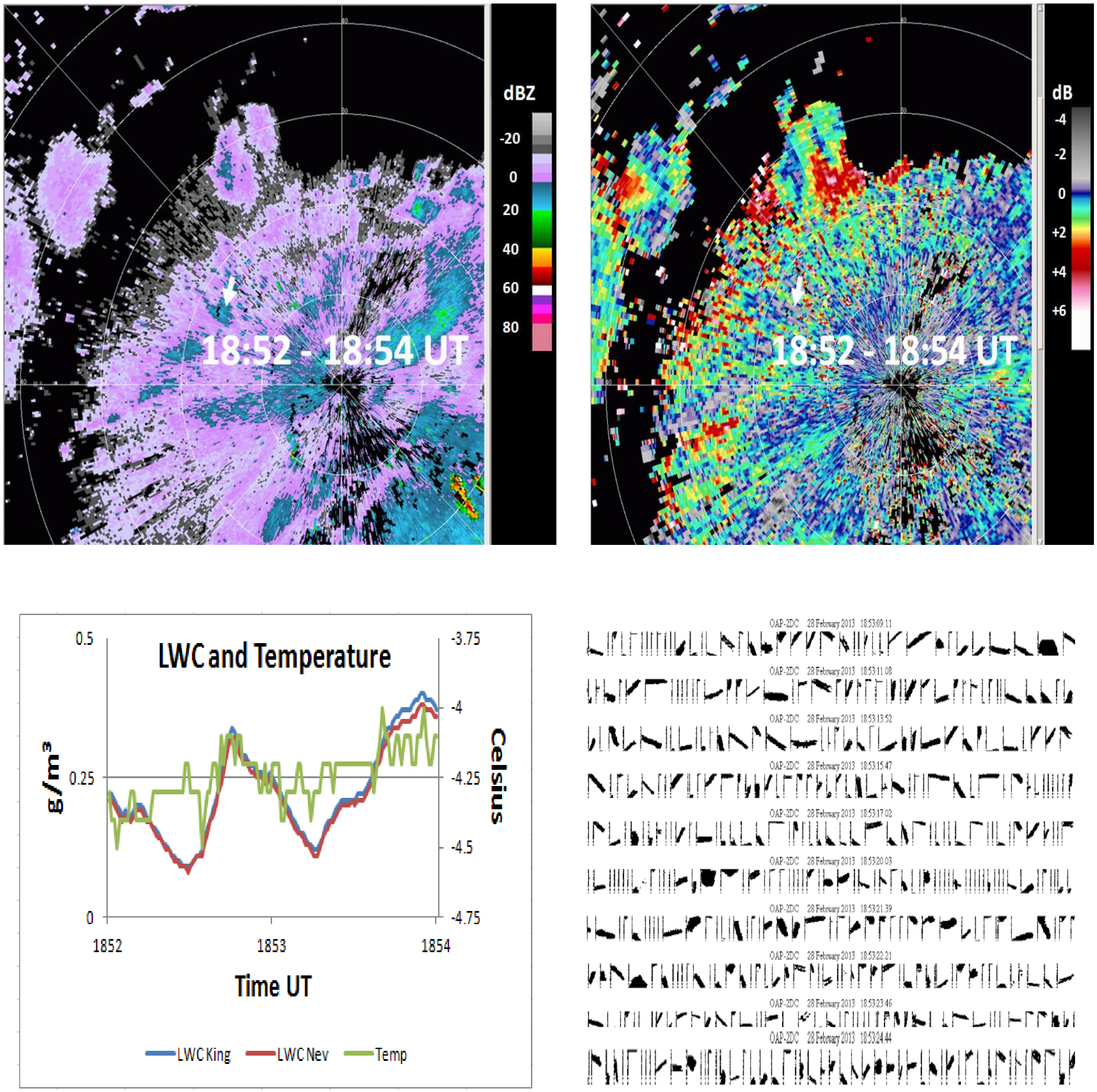

Figure 10. Four-panel plot documenting the Convair aircraft sample time interval 1852-1854 UTC, and including space-time-matched KBUF radar reflectivity Z (upper left), differential reflectivity ZDR (upper right), in situ liquid water content (g/m^3) and temperature (^{o}C) (lower left), and ice particle PMS 2DC imagery (lower right), with pixel resolution 25 µm and spacing between vertical lines 800 µm. Needles are the predominant hydrometeor type at this time, and the co-located ZDR values are 0 to +4 dB. Some needles appear to be rimed. Z and ZDR panel for elevation angle 0.5^o with range ring labels in nautical miles.

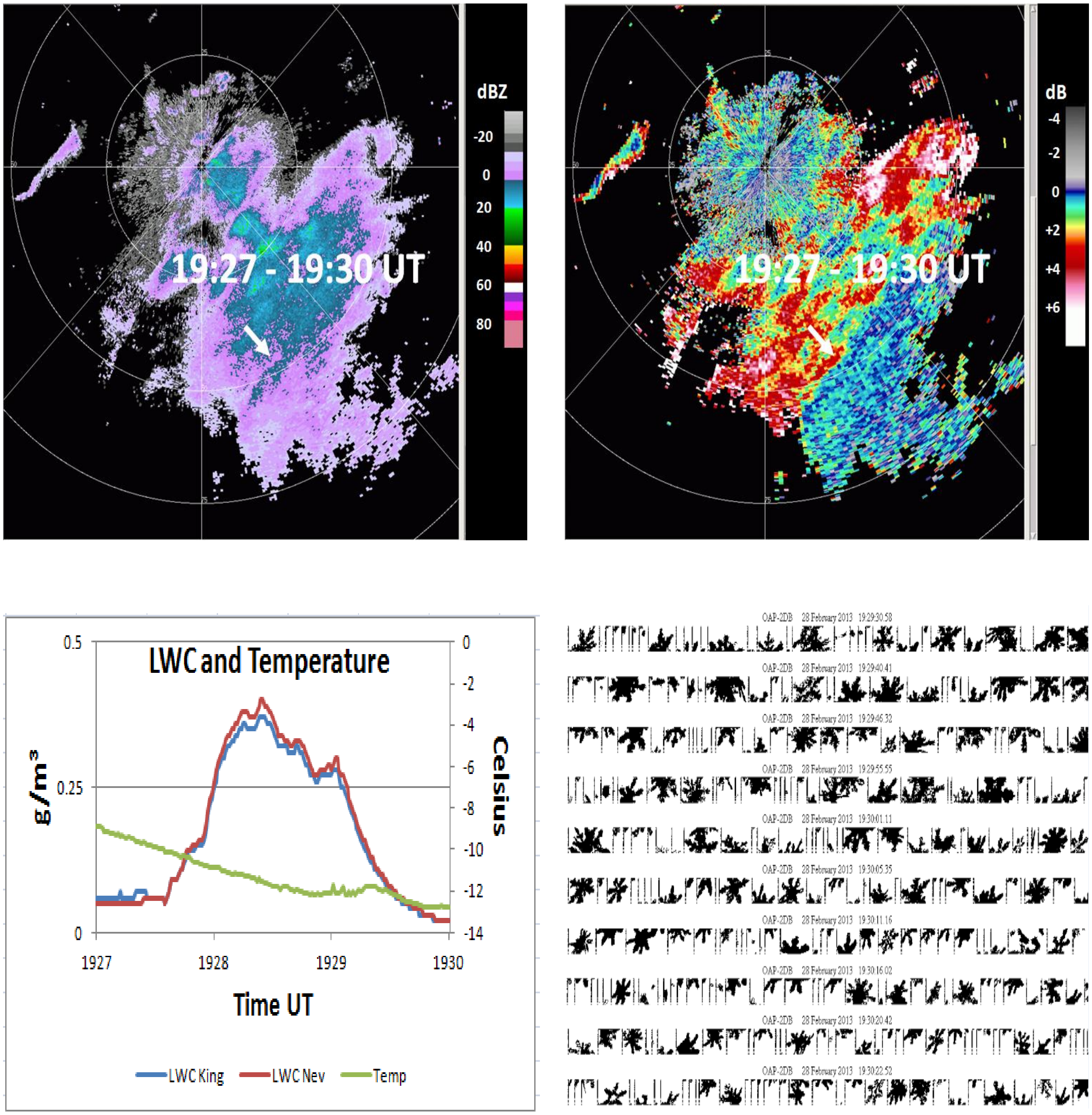

Figure 11. Four-panel plot documenting the Convair aircraft sample time interval 1927-1930 UTC, and including space-time-matched KBUF radar reflectivity Z (upper left), differential reflectivity ZDR (upper right), in situ liquid water content (g/m^3) and temperature (^{o}C) (lower left), and ice particle PMS 2DB imagery (lower right), with pixel resolution 50 µm and spacing between vertical lines 1600 µm. Dendritic crystals and aggregates are the predominant hydrometeor type at this time, and the co-located ZDR values are +2 to +7 dB. Riming of crystals is expected but difficult to discern. Z and ZDR panel for elevation angle 1.5^o with range ring labels in nautical miles.

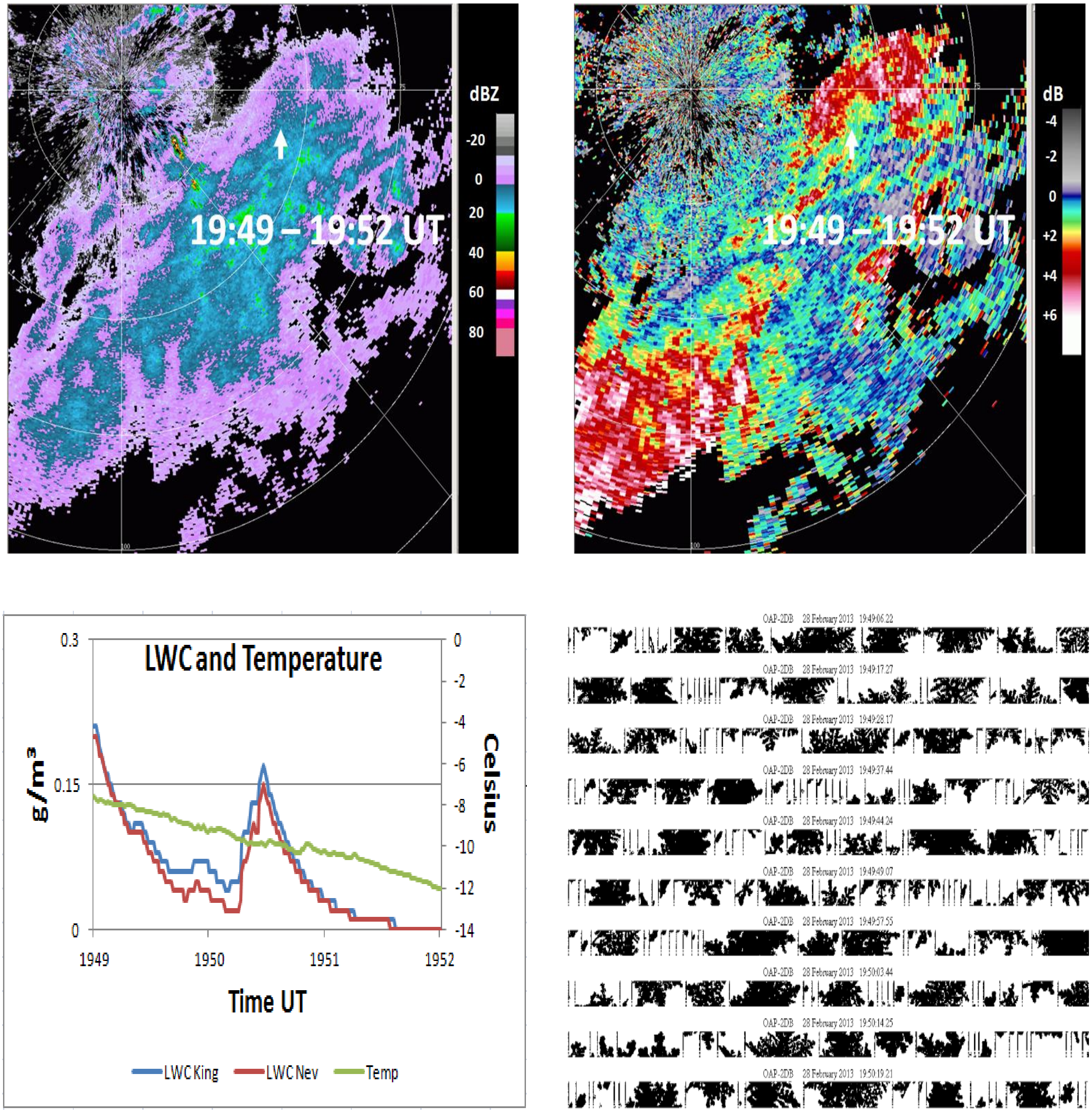

Figure 12. Four-panel plot documenting the Convair aircraft sample time interval 1949-1952 UTC, and including space-time-matched KBUF radar reflectivity Z (upper left), differential reflectivity ZDR (upper right), in situ liquid water content (g/m^3) and temperature (^{o}C) (lower left), and ice particle PMS 2DB imagery (lower right), with pixel resolution 50 µm and spacing between vertical lines 1600 µm. Dendritic crystals and aggregates are the predominant hydrometeor type at this time, and the co-located ZDR values are +1 to +5 dB. Z and ZDR panel for elevation angle 0.5^o with range ring labels in nautical miles.